Highly doped semiconductor plasmonic nanoantenna arrays for polarization selective broadband surface-enhanced infrared absorption spectroscopy of vanillin

Franziska B. Barho, Fernando Gonzalez-Posada, Maria-Jose Milla, Mario Bomers, Laurent Cerutti, Eric Tournié, Thierry Taliercio

Research article

Franziska B. Barho*, Fernando Gonzalez-Posada, Maria-Jose Milla, Mario Bomers, Laurent Cerutti, Eric Tournié and Thierry Taliercio

Highly doped semiconductor plasmonic nanoantenna arrays for polarization selective broadband surface-enhanced infrared absorption spectroscopy of vanillin

https://doi.org/10.1515/nanoph-2017-0052
Received May 15, 2017; revised July 27, 2017; accepted August 11, 2017

Abstract: Tailored plasmonic nanoantennas are needed for diverse applications, among those sensing. Surface-enhanced infrared absorption (SEIRA) spectroscopy using adapted nanoantenna substrates is an efficient technique for the selective detection of molecules by their vibrational spectra, even in small quantity. Highly doped semiconductors have been proposed as innovative materials for plasmonics, especially for more flexibility concerning the targeted spectral range. Here, we report on rectangular-shaped, highly Si-doped InAsSb nanoantennas sustaining polarization switchable longitudinal and transverse plasmonic resonances in the mid-infrared. For small array periodicities, the highest reflectance intensity is obtained. Large periodicities can be used to combine localized surface plasmon resonances (SPR) with array resonances, as shown in electromagnetic calculations. The nanoantenna arrays can be efficiently used for broadband SEIRA spectroscopy, exploiting the spectral overlap between the large longitudinal or transverse plasmonic resonances and narrow infrared active absorption features of an analyte molecule. We demonstrate an increase of the vibrational line intensity up to a factor of 5.7 of infrared-active absorption features of vanillin in the fingerprint spectral region, yielding enhancement factors of three to four orders of magnitude. Moreover, an optimized readout for SPR sensing is proposed based on slightly overlapping longitudinal and transverse localized SPR.

Keywords: highly doped semiconductors; nanostructures; plasmonics; SEIRA; sensing; SPR; vibrational spectroscopy.

***Corresponding author: Franziska B. Barho,** IES, Université de Montpellier, CNRS, Montpellier, France.
e-mail: franziska.barho@umontpellier.fr.
http://orcid.org/0000-0003-4502-0702
Fernando Gonzalez-Posada, Maria-Jose Milla, Mario Bomers, Laurent Cerutti, Eric Tournié and Thierry Taliercio: IES, Université de Montpellier, CNRS, Montpellier, France

1 Introduction

Surfaces with adjustable optical properties are extensively studied and of interest for sensing [1–4], controlled light absorption [5], color printing [6–8], among other applications. Plasmonics is one approach to enable special optical properties, like intense reflection, absorption or transmission in a targeted wavelength range. Surface plasmon polaritons, coherent oscillations of the electron density coupled to an electromagnetic wave, can be excited at interfaces between metals and dielectrics, or in metallic particles due to the confinement of the electrons within the particle boundaries. Notably, the choice of size and shape for tailored nanoparticles allows us to control the localized surface plasmon resonance (LSPR) wavelength within the limits imposed by intrinsic material properties. By means of modern nanofabrication methods, surfaces with tailored and arranged nanoparticles acting as optical antenna [9–11] can be fabricated.

While numerous studies have been carried out on metallic nanoantennas, either as individual objects [12–17], or organized in arrays [1, 10, 18–21], semiconductor plasmonic nanoantenna surfaces have rarely been investigated [22], especially in ordered array arrangements [23–25]. Highly doped semiconductors (HDSC) have been introduced as engineered metals or "designed metals" for plasmonics [22, 23] as they offer the possibility of tuning the plasma frequency, an intrinsic parameter for traditional metals, via the doping level. Doping densities of several 10^{19} cm^{-3} have been reported for InAs [23], and densities up to 10^{20} cm^{-3} have been predicted [26]. For the epitaxial growth of InAs on GaSb substrates, the incorporation of a few percent of Sb allows an improved crystalline quality due to the lattice-matched growth conditions [27] while the possibility of high carrier incorporation as in InAs is maintained. For high doping densities and due to the small effective electron mass, plasma wavelengths of 4 μm can be reached for InAs [23], making it and the lattice-matched alloy InAsSb for GaSb substrates ideal plasmonic materials for the mid-infrared (IR) spectral range.

The tunable plasma frequency of HDSC constitutes an additional degree of freedom besides the geometric arrangement of plasmonic resonators and might be beneficial to obtain designed optical properties. In contrast, gold or more generally noble metal nanoantennas for the near to mid-IR spectral range have to rely only on shape and geometric arrangement to obtain resonances in a targeted spectral range as their plasma frequency, in the UV spectral range [28], is constant. Typically, the noble metal nanoantennas for the mid-IR have high aspect ratios, making them the optical analogue to micro- and radiowave dipole antennas but with slightly modified scaling rules [11, 13, 29]. They benefit furthermore from the lightning rod effect, the geometrical electric field enhancement at highly curved surfaces [30]. Antenna dimers with nanometer size gaps have been employed to further increase the electric field enhancement and focus incident light into small hot spots [12, 16, 31, 32]. The use of HDSC allows us to deviate from these design schemes, owing to the material properties, as the elongated shape or the interaction through a gap to decrease the resonance frequency is not necessarily needed to reach resonance frequencies in the mid-IR. This opens the way to simpler nanoantenna designs without gaps or high curvature.

In this article, we investigate ordered arrays of rectangular-shaped plasmonic nanoantennas fabricated from highly doped InAsSb epitaxial layers on a GaSb substrate. Due to its plasma frequency in the mid-IR spectral range, plasmonic resonances of highly doped InAsSb lie naturally in the mid-IR and are accompanied by high electric field enhancement compared to gold [33]. The rectangular shape generates polarization selective plasmonic resonances. Arrays with different periodicities are studied experimentally and by finite-difference time-domain (FDTD) calculations in order to estimate the interaction range between resonators. The optical response of the sub-micrometric nanoantennas spaced of at least their size in the array varies only in intensity for different periodicities. Hence, the antennas are uncoupled, which is linked to the weak contribution from scattering to their extinction. An effect from the array can however be evidenced when the grating periodicity is large enough for diffractive modes to become radiative and when they are spectrally tuned to the LSPR sustained by the nanoantennas. The original approach in this article is to cover a large spectral range by the polarization switchable plasmonic resonances in simple, gap-free rectangular nanoantennas. This is particularly interesting for sensing applications, like resonant surface-enhanced infrared absorption (SEIRA) spectroscopy, which ideally requires a good spectral overlap between the plasmonic resonance and the narrow IR-active molecular vibrations [15, 32]. The spectral overlap can easily be achieved by selecting the spectral band of interest by the polarization of the incident light, offering a new degree of freedom for the tuning of the resonances. As a case study, we demonstrate broadband SEIRA with vanillin as an exemplary analyte. The vanillin molecule displays several molecular vibration characteristics of the substituted aromatic ring at wavelengths in the mid-IR. An increase in the signal intensity of the vibrational features of factors up to 5.7 is obtained. Considering the active zones for surface enhancement in proximity of the nanoantenna corners, enhancement factors of 10^3 to 10^4 are achieved. Finally, an optimized readout for intensity-based surface plasmon resonance (SPR) sensing is proposed, exploiting the polarization selective resonances.

2 Experimental details

Plasmonic nanoantenna arrays are fabricated from 100-nm-thin epitaxial, Si-doped $InAs_{0.91}Sb_{0.09}$ films grown lattice matched on a 200-nm-thick GaSb buffer layer on the GaSb substrate. The doping level of the InAsSb film is 5.1×10^{19} cm^{-3} corresponding to a plasma wavelength $\lambda_p = 5.35$ µm [34]. The buffer layer is non-intentionally doped, and the GaSb substrate is n-type, Te-doped at a level of 8×10^{17} cm^{-3}. Patterns are defined by standard UV lithography using dilute AZ MIR 701 photoresist. Rectangular patterns are obtained by superposition of two line patterns rotated by 90°. After development of the photoresist, the InAsSb film is chemically etched with $C_6H_8O_7$:H_2O_2 [35]. Photoresist is then removed with acetone, and the samples are cleaned with isopropanol and dried under N_2 flow. The plasmonic nanoantennas are rectangular shaped with slightly rounded corners due to the proximity effect in the double lithographic exposure. A scanning electron microscope image of the surface is shown in Figure 1A. Figure 1B displays a scheme of the nanoantenna array with the axes reference used in the following to designate the polarization directions with respect to the nanoantenna axes.

IR spectroscopy of plasmonic nanoantenna samples is performed using an Hyperion 3000 IR microscope coupled to a Vertex 70 Fourier-transform IR spectrometer. A globar light source is used. The light is focused on the sample by a Cassegrain objective (15× magnification) with $NA = 0.4$ and detected by a mercury cadmium telluride detector in the spectral range of 5500–450 cm^{-1}. The acquired spectra are normalized to the spectrum of a gold mirror serving as reference.

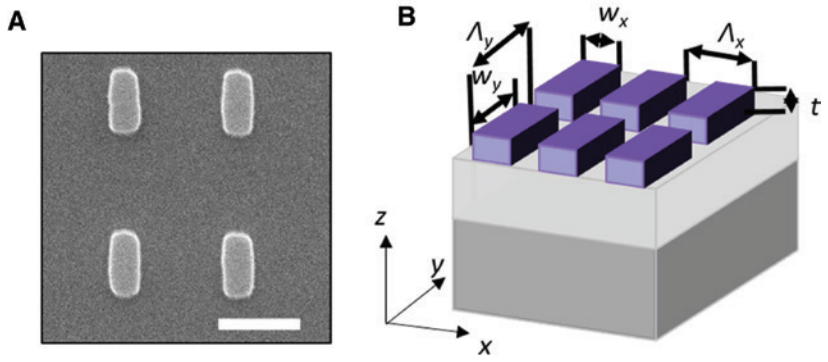

Figure 1: Arrays of highly doped InAsSb nanoantennas on GaSb substrates for SEIRA spectroscopy.
(A) SEM image of the nanoantennas. Scale bar is 1 µm. (B) Schematic of the nanoantenna array.

3 Optical characterization

In consequence of the anisotropy of the side lengths of the rectangular nanoantennas, a strong polarization dependence of the optical response is expected [36, 37]. Figure 2 displays the reflectance spectra of an array with periodicities $\Lambda_x = 1.4$ µm, $\Lambda_y = 2.0$ µm of resonators with side lengths $w_x = 400 \pm 30$ nm and $w_y = 810 \pm 30$ nm, obtained with unpolarized and polarized light. Under *y* polarization, one strong reflectance peak is revealed at $\lambda_l = 16.8$ µm, attributed to the longitudinal LSPR of the resonators, whereas two peaks are observed under *x* polarization, at $\lambda_t = 11.7$ µm and $\lambda_t' = 10.4$ µm. The origin of this particular line shape under *x* polarization is linked to higher order excitations and the aspect ratio of the resonators. In *y* polarization, the peak at a short wavelength appears in simulations as a weak feature relatively far from the principal LSPR but is experimentally below the noise level. The transverse LSPR, associated with the short axis of the resonator, are at a smaller wavelength than the longitudinal LSPR [18]. The reflectance intensity is weaker, due to the smaller dipole moment, or higher depolarization factor, of the transverse LSPR [18, 20, 38].

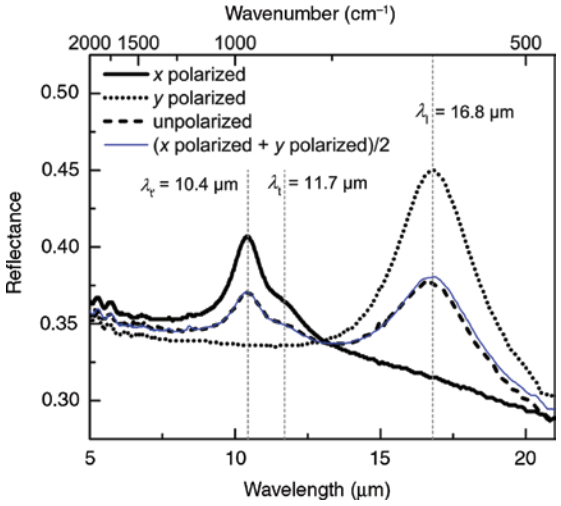

Figure 2: Experimental reflectance spectra of the rectangular nanoantenna array with the electric field vector perpendicular (black solid line, *x* polarized) or parallel (black dotted line, *y* polarized) to the long axis of the resonator, respectively, unpolarized light (black dashed line).
The weighted sum of the spectra under *x* and *y* polarization is also shown (blue thin line).

Next, we investigate the transition between the excitation of the longitudinal or transverse LSPR using intermediate polarizations not aligned with the main axes. The polarization angle Θ between the *y* axis (long axis of the rectangular nanoantennas) and the polarization vector is varied in steps of π/16 rad. From the measured reflectance spectra, the longitudinal and transverse LSPR wavelengths were extracted and the intensity value at these wavelengths was plotted against the polarization angle Θ (Figure 3). Note that a baseline correction was performed to extract the variation of the LSPR intensity without considering the reflection from the substrate. Therefore, the reflectance of a bare GaSb substrate at the investigated longitudinal and transverse resonance wavelengths was subtracted. Figure 3 indicates that by changing the polarization, it is possible to switch between the longitudinal and transverse LSPR. The intensity of the longitudinal resonance decreases while the transverse resonances become more pronounced when increasing the polarization angle from 0° to 90°. The transition between the limiting cases can be fitted by cosine squared functions, with the maximum reflectance value extracted from the measurement. The dipole-like pattern in the polar plot confirms the polarization dependence [39]. The polarization vector can be decomposed into components parallel and perpendicular to the long axis of the nanoantenna. When

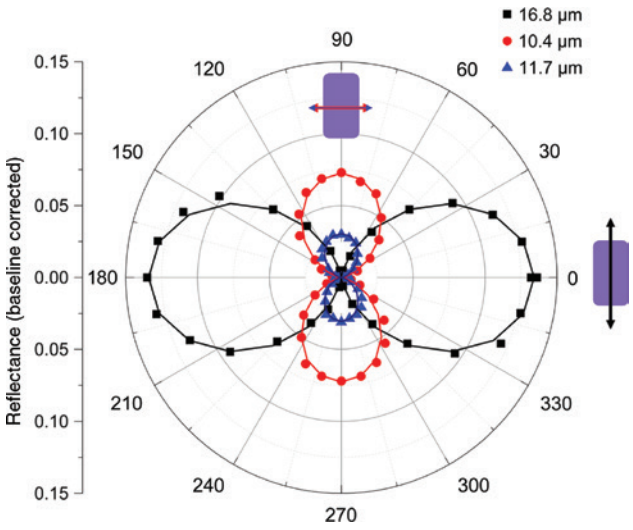

Figure 3: Polar plot of the reflectance intensity at 10.4 µm, 11.7 µm and 16.8 µm, corresponding to the LSPR wavelengths in *x* and *y* polarizations, against polarization angle, defined as the angle between the electric field vector and the long axis of the rectangular resonators. Solid lines are functions of the form $R_{max}\cos^2(\alpha)$, with R_{max} fitted to the measurement.

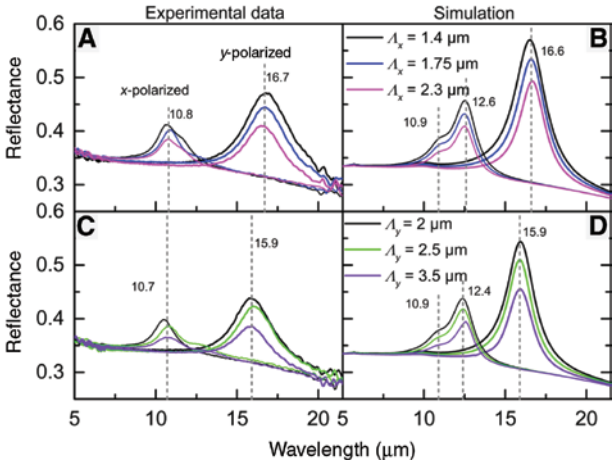

Figure 4: Experimental (A, C) and simulated (B, D) reflectance spectra of rectangular nanoantennas.
(A and B) Variation of the periodicity in the *x* direction. The periodicity in the *y* direction is fixed (2 µm). Measured nanoantenna dimensions are $w_x = 450 \pm 30$ nm, $w_y = 830 \pm 30$ nm; in simulations $w_x = 450$ nm, $w_y = 830$ nm were used. (C and D) Variation of the periodicity in the *y* direction. The periodicity in the *x* direction is fixed (1.4 µm). Measured nanoantenna dimensions are $w_x = 430 \pm 30$ nm, $w_y = 760 \pm 30$ nm; in simulations $w_x = 430$ nm, $w_y = 760$ nm.

the component is large, the associated resonance is strong. Using an intermediate polarization direction or unpolarized light as it has been shown in Figure 2, it is possible to excite simultaneously both LSPR as a superposition of the orthogonal polarization directions. This can be applied when it is needed to cover a large spectral range.

Interestingly, both LSPR lie in the IR spectral range and can thus be exploited for resonant SEIRA for broadband identification, as will be shown below. In comparison, a typical gold nanorod antenna with resonances in the IR displays transverse resonances in another spectral range [38] due to its high aspect ratio, or the transverse resonance is below the noise level [13], so that only the longitudinal resonance can effectively be used for resonant SEIRA.

4 Interaction range in highly doped InAsSb nanoantenna arrays

Several nanoantenna arrays with different periods in the *x* and *y* directions were fabricated in order to investigate the influence of the array arrangement. Figure 4A displays the reflectance spectra of nanoantennas with dimensions $w_x = 450 \pm 30$ nm, $w_y = 830 \pm 30$ nm and varying periods in the *x* direction. The periodicity in the *y* direction is kept constant at 2 µm. A decrease of the reflectance maxima in either polarization direction is observed due to the lower density of nanoantennas on the surface. However, the spectral positions of the resonances are not influenced by the periodicity. The slight fluctuations are likely attributed to the uncertainty on the nanoantenna dimensions. Similar observations are obtained for variation of the period in the *y* direction (Figure 4C). In this case, the resonator dimensions are $w_x = 430 \pm 30$ nm, $w_y = 760 \pm 30$ nm and the constant periodicity in the *x* direction is 1.4 µm.

Our experimental measurements are supported by 3D FDTD calculations [40]. One unit cell, including all symmetry planes, is modeled. The array arrangement is implemented by periodic boundary conditions. The spectral range from 1 to 25 µm is investigated under normal incidence of light. The average nanoantenna sizes indicated above from the fabricated samples were used (model for the variation of the transverse period: $w_x = 450$ nm, $w_y = 830$ nm; variation of the longitudinal period: $w_x = 430$ nm, $w_y = 760$ nm). We use slightly rounded corners for the resonator geometry with a curvature radius of 20 nm to exclude effects from sharp tips. Mesh size inside the nanoantenna and surrounding all its interfaces to the substrate and the air is 5 nm. The highly doped InAsSb is modeled by a Drude dielectric function:

$$\varepsilon(\omega) = \varepsilon_\infty \left(1 - \frac{\omega_p}{\omega^2 + i\gamma\omega}\right),$$

with the high-frequency dielectric constant $\varepsilon_\infty = 10.4$, the plasma frequency $\omega_p = 3.588 \times 10^{14}$ rad s^{-1}, and the

damping parameter $\gamma = 1 \times 10^{13}$ rad s^{-1}. The plasma frequency is chosen according to the experimental measurements of the plasma wavelength of the samples, and the damping parameter has been extracted from reflectance measurements on uncorrugated InAsSb layers [34]. As the GaSb substrate is slightly doped and becomes transparent at around 40 μm, it is also modeled by a Drude dielectric function with the following parameters: $\varepsilon_\infty = 14.2129$, $\omega_p = 4.629 \times 10^{14}$ rad s^{-1}, and $\gamma = 5 \times 10^{12}$ rad s^{-1}.

In contrast to the simulations, in experimental measurements the intensity of the short wavelength transverse resonance is higher than the longer wavelength transverse resonance. The transverse LSPR at a longer wavelength seems to be strongly sensitive to the actual shape of the nanoantennas and is most visible if the resonator corners are accentuated. The investigation of the line shape depending on the exact nanoantenna shape goes beyond the scope of this article.

Figure 4B (D) confirms in simulation the decrease in the intensity of both longitudinal and transverse LSPR when the periodicity increases in the x (y) direction. We do not have evidence of spectral shifting of the LSPR depending on the period in the investigated range of array periodicities, in simulation under the condition of identical dimensions for the resonators. We deduce that the electromagnetic coupling between nanoantennas is negligible. The nanoantennas act as independent objects for the investigated range of periodicities. The reason for this will be discussed below.

Different interaction regimes in nanoparticle arrays have been identified in the literature, based mainly on examples of metallic, often Au and Ag nanoparticles [41–46]. Near-field interactions arise for gaps between antennas in the range of several tenths of nanometers. These spacings being small compared to optical and IR wavelengths, the interaction is often treated in an electrostatic framework of coupled dipoles [43], or alternatively by the plasmon hybridization model [44]. Near-field interactions can be excluded for the presented HDSC nanoantenna arrays as the spacing between antennas is in the micrometric range.

Long-range far-field interactions occur due to the scattered field of each resonator in the array, leading eventually to constructive and destructive interference. To further investigate the origin of the insensitivity to long-range interaction in the antenna arrays, we calculated the scattering and absorption cross-sections for a single nanoantenna (see Supplementary Figure S1), exemplary with the lateral dimensions as in Figure 4A and B. The main contribution to the extinction comes from absorption, while scattering contributes clearly less. Consequently, the radiated power of the antennas is small, which reduces the antenna interaction [47]. This allows us to densify the nanoantennas in arrays while maintaining the resonance quality. We now investigate under which conditions long-range, far-field interaction can become apparent.

Diffractive modes propagating at the substrate interface of the grating become radiative when the period $\Lambda = \lambda_{eff} = \lambda/n$, with the incident-free space wavelength λ and the refractive index n of the substrate. When $\lambda_{eff} > \Lambda$, only the zeroth-order diffraction appears and the higher orders are non-radiative. But when $\Lambda \geq \lambda_{eff}$, diffractive far-field interaction can arise [41, 42, 46]. However, the effect might be weak in the HDSC nanoantenna arrays, as the scattering is reduced compared to the nonradiative decay channel as shown above. When tuning diffractive modes to be spectrally aligned with the LSPR, they become nevertheless apparent, as evidenced in simulations. In Figure 5, the arrays with diffractive modes spectrally tuned to the transverse (A) or longitudinal (B) resonance are compared to arrays where diffractive modes are not aligned with the LSPR and where, consequently, these weak features are not or scarcely visible. An estimation for the investigated resonances with $n_{substrate} = \sqrt{\varepsilon_\infty} = 3.77$ yields $\Lambda_x = 2.9$ μm and 3.3 μm to have diffractive modes spectrally tuned to the

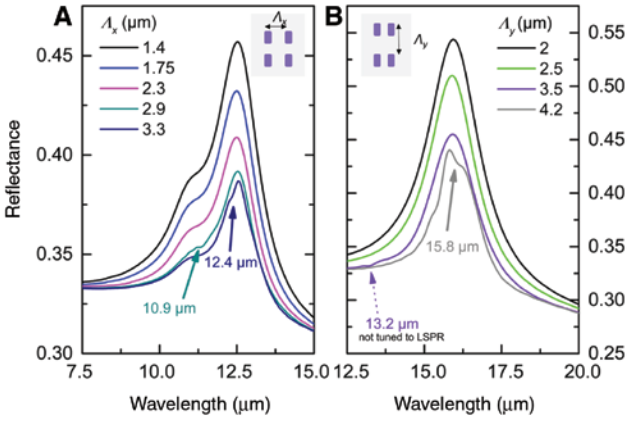

Figure 5: Simulated reflectance spectra of rectangular nanoantenna arrays with large periodicity with a diffractive grating mode spectrally tuned to the LSPR peak.
For comparison, the spectra from Figure 4B and D are shown where the diffractive modes are not tuned to the LSPR. (A) Variation of the transverse periodicity Λ_x. Only the transverse LSPR is shown. Values of the periodicity are chosen so that diffractive modes at the array-substrate interface propagating in the x direction are spectrally tuned to the transverse (x polarized) resonances. Arrows indicate the wavelengths where the diffractive modes can be observed. (B) Variation of the longitudinal periodicity Λ_y. The periodicity was chosen to obtain the diffractive mode propagating in the y direction in resonance with the longitudinal (y polarized) resonance. Note that a feature appears for the grating with a periodicity of 3.5 μm at 13.2 μm, indicated by the dashed arrow, which is weakly visible compared to the diffractive feature in resonance with the LSPR for the periodicity 4.2 μm.

transverse resonances or $\Lambda_y = 4.2$ µm to have a diffractive mode tuned to the longitudinal resonance at 15.9 µm.

Combining individual LSPR with array resonances has been proven to be beneficial to enhance the sensitivity in gold nanoantenna arrays [1]. Similarly, we demonstrate here the spectral superposition of LSPR and array resonances in HDSC arrays for rather large periodicities. However, the size relation between the nanoantenna dimensions and the necessary array periodicity is different, as the resonators can be much smaller yet sustaining resonances at long wavelengths due to the low plasma frequency compared to noble metals. As has been indicated in Figure 4, densifying the nanoantennas on arrays with smaller periodicities leads to stronger reflectance intensity. This densification is possibly beneficial compared to the large array periodicities necessary for the diffractive orders to become radiative, in this particular case of relatively small-sized nanoantennas with long wavelength resonances. Especially, a high densification with unaltered resonance quality should be possible due to the weak contribution of scattering to the extinction [47].

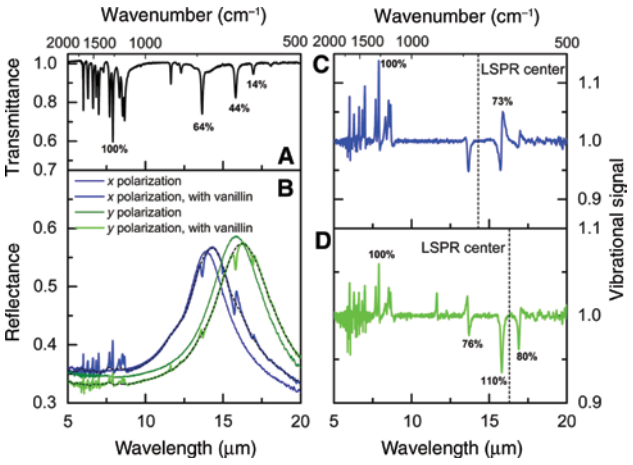

Figure 6: (A) Transmittance spectrum of vanillin, shown as a reference. (B) Reflectance spectra of the nanoantenna array covered with vanillin (thick lines). Thin lines are spectra before vanillin deposition on the same sample position. The black dashed lines are fits using Eiler's smoothing algorithm, excluding the vibrational features. The Fano line shape of the vibrational features spectrally covered by the large LSPR evidences the coupling between the LSPR and the narrow vibrational lines. The sample size area was 150 × 150 µm². In this area, around 11,500 antennas are located. (C) Measured data in *x* polarization normalized to Eiler's fit. Percentage values indicate the signal strength with respect to the reference line at 7.9 µm to which an intensity of 100% was assigned. The LSPR center wavelength is indicated (black dashed line). (D) Measured data in *y* polarization normalized to Eiler's fit. Percentage values are indicated for lines with significant enhancement compared to the reference spectrum (more than 10 percentage points increase compared to the relative intensities in the reference spectrum).

5 Resonant SEIRA and SPR sensing demonstration

Within the last decade, it has been explored that SEIRA can be improved when resonant, tailored nanoantennas are used [48], instead of rough metallic surfaces where the effect has initially been discovered [49]. The polarization selective resonances of the investigated HDSC nanoantennas are particularly suitable for resonant SEIRA spectroscopy at mid-IR wavelengths. The condition of the resonant tuning between the large plasmonic resonance and the narrow IR absorption features of molecules is fulfilled at two center wavelengths and covers several absorption features close to the longitudinal and transverse resonance wavelengths, especially on the long wavelength side of the resonance maximum [50].

As a case study for SEIRA and SPR, we used vanillin (4-hydroxy-3-methoxybenzaldehyde) as an analyte molecule. Vanillin is the major compound of the vanilla bean [51] and can be chemically synthetized for mass production. It finds applications in food, pharmaceuticals and perfumery [52]. The transmittance spectrum of vanillin, shown in Figure 6A, features several strong IR-active vibrational lines of the functional groups present in the molecule as well as the characteristic vibrations of the substituted benzene nucleus in the fingerprint region from 1500 to 500 cm^{-1} [53] that are intended to be detected using the nanoantenna arrays. A transmittance spectrum of vanillin was obtained from a high concentrated solution (50 mg/mL) deposited on a transparent KBr platelet. The spectrum was normalized to the one of a clean KBr platelet.

5.1 SEIRA

For the resonant SEIRA demonstration, a nanoantenna array with dimensions $w_x = 540 \pm 30$ nm and $w_y = 600 \pm 40$ nm on a square array of 1.4 µm × 1.4 µm was chosen. The transverse and longitudinal modes display a partial spectral overlap for this nanoantenna geometry. The spectral range of the fingerprint vibrations is covered by the plasmonic resonances, while the vibrations at shorter wavelength can be used as a reference for the strength of the vibrations. Vanillin was dissolved in ethanol with a concentration of 2 mg/mL. Then, a droplet of few µL was deposited on the sample surface and the solvent was evaporated. Around 10 nmol are thus

deposited on the sample, the molecular mass of vanillin being 152.1 g/mol. Assuming a homogeneous distribution of the vanillin molecules on the sample surface of approximately 1 cm^2, 0.5 ng of vanillin is located within the zone of 150×150 μm^2 from which the reflectance signal is measured. This yields 12 femtogram per antenna, if we consider the antenna surface area, and thus 5×10^7 molecules per antenna. The number of molecules is three orders of magnitude higher than the best reported value for the detection of octadecanethiol self-assembled monolayers with a gold nanorod antenna [48]. Reflectance measurements were performed on the same sample position on the bare sample and subsequently on the sample covered with vanillin. Figure 6B displays the reflectance curves for the orthogonal polarization directions allowing the excitation of either the longitudinal or the transverse LSPR. For both polarizations, several vibrational lines lie within the spectral band covered and thus interact with the large plasmonic resonance. This can be seen from the Fano line shape of the vibrational lines in this spectral range [54].

In order to evaluate the signal enhancement, the measured reflectance curves were fitted using the smoothing algorithm proposed by Eilers [55] (dashed lines in Figure 6B), excluding the vibrational signals. Then, the fit was used as a background signal to normalize the measured data to it. Thus, a mainly flat line but for the vibrational signals is obtained (Figure 6C and D), allowing us to compare the signal strengths in spectral ranges where plasmonic enhancement is expected to not impacted spectral ranges. The vibrational signal strength is obtained from this baseline corrected spectrum by a readout of the peak-to-peak value of the vibrational signals.

To assess the increase of the vibrational signal strength, we first obtained the relative intensities from the reference transmittance spectrum of vanillin for the vibrational features at 13.65, 15.81 and 16.95 μm. Intensities are given as percent of the strongest vibrational feature at 7.9 μm, attributed to the C–O stretching vibration of the vanillin molecule. Then, we proceeded analogously for the vibrational signals obtained on the nanoantenna array. The percentage values are indicated in Figure 6C and D for the lines where a significant enhancement of more than 10 percentage points compared to the reference spectrum is obtained. The comparison to the non-enhanced lines at a lower wavelength allows us to ensure that an identical number of molecules contribute to the signal in each of the measurements shown.

Not assessed were chemical effects and the molecular orientation on the different surfaces [53], namely the KBr platelet for the reference transmission measurements or the nanoantenna array, so that we considered only the significantly enhanced lines in the evaluation. Moreover, some line intensities might be reduced, due to the direct absorption of the vanillin, because direct absorption produces peaks in the reflectance spectra, whereas the Fano-type interaction with the plasmonic nanoantenna is here at the origin of an electromagnetic-induced transparency, seen as dip in the reflectance spectra. An enhancement can be observed when the electromagnetic effect outbalances the direct absorption.

For further comparison between the reference spectrum and the measurements on the nanoantenna arrays, the relative signal intensity increase was calculated by taking the ratio of the enhanced signals to the reference signal at the investigated wavelengths. Values range from 1.2 to 5.7 and are indicated in Table 1 associated with each vibrational line.

The enhanced signals originate mainly from the zone of maximum field enhancement close to the nanoantennas. Considering this, we may estimate the enhancement factor achieved through the use of the plasmonic structure, given by [48]

$$\mathrm{EF} = \frac{I_{\mathrm{SEIRA}}}{I_0} \frac{A_0}{A_{\mathrm{SEIRA}}},$$

where I_{SEIRA} is the enhanced vibrational signal strength, I_0 is the strength of the unenhanced signal, A_0 is the area covered with molecules and A_{SEIRA} is the active surface where high field enhancement is achieved.

From the electric field profiles shown in Supplementary Figure S2, it can be found that the electric field is strongest near the nanoantenna corners. The sectional view (Supplementary Figure S2B) indicates that the field is especially enhanced on the substrate-antenna interface. For simplicity, we consider the field distribution particularly in the plane close to the interface shown in Supplementary Figure S2A, even if in some other planes there is less enhancement. We estimate the active surface A_{SEIRA} per unit cell area A_0 corresponding to a square of 20 nm side length at each corner. Only approximately half of the surface of the squares is accessible to the analyte, the other part being situated inside the nanoantenna. This active surface corresponds to 0.4‰ of the unit cell area. Enhancement factors from 2900 to 14,000 are obtained, as indicated in Table 1. This is one to two orders of magnitude higher than what has been reported for Ge nanoantennas, exploiting additionally a hotspot in a gap between nanoantennas [24] and is in the range of enhancement factors for noble metal nanoantennas found in other studies which range from 1000 to 100,000 depending on

Table 1: Summary of the signal increase compared to the reference transmittance spectrum of vanillin and the enhancement factors accounting for the active zone.

Wavelength/µm (wavenumber/cm^{-1})	Intensity in reference transmittance spectrum as % of strongest line	Vibrational signal strength (*x* polarized) as % of reference line	Signal increase compared to reference transmittance spectrum (I_{SEIRA}/I_0)	Enhancement factor	Vibrational signal strength (*y* polarized) as % of reference line	Signal increase compared to reference transmittance spectrum (I_{SEIRA}/I_0)	Enhancement factor
7.9 (1266)	100	100	Normalized		100	Normalized	
13.6 (733)	64				76	1.2	2900
15.8 (633)	44	73	1.7	4200	110	2.5	6100
16.9 (590)	14				80	5.7	14,000

The reference line is the C–O stretching vibration at 7.9 µm.

the antenna shape, material and arrangement [48]. As already mentioned, the proposed semiconductor nanoantenna array in the investigated geometrical configuration does not exploit confinement in gaps or the lightning rod effect which is stronger at high aspect ratio nanoantennas, so that there is potential to reach even higher enhancement factors when these more sophisticated geometries are employed.

5.2 SPR

Furthermore, the resonator array with partially overlapping orthogonal resonances offers the possibility of optimizing the measured signal in SPR-sensing devices [56]. SPR sensing exploits the modification of the refractive index due to the presence of molecules to detect the analyte. As plasmonic resonances are sensitive to the refractive index, they will convert the refractive index modification into an optically measurable signal. In a previous work, SPR sensing with highly doped InAsSb plasmonic nanostructures based on a readout of the wavelength shift upon refractive index modification was assessed [33]. SPR sensing with simple instrumentation relies on the change in intensity, under illumination with a monochromatic light source and measured by a photodiode [57], typically at the wavelength of the initial resonance maximum or in the shoulder of the resonance peak. When the ideally narrow resonance shifts upon modification of the refractive index, the intensity decreases, especially

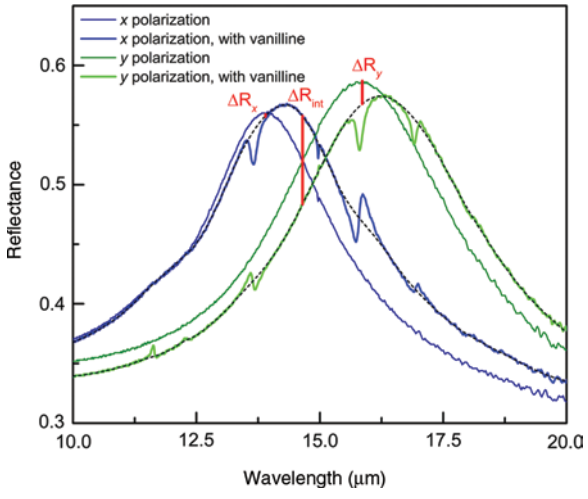

Figure 7: Detail of Figure 6B.
The signal strengths for SPR sensing with an intensity-based readout at the wavelengths corresponding to the maximum of the transverse resonance (ΔR_x), of the longitudinal resonance (ΔR_y) and the intersection point (ΔR_{int}) are highlighted by the red lines.

when the resonance is moved largely out of the measured wavelength. Using an evaluation in this manner, we obtain a measured signal of $\Delta R = 0.001$ ($\Delta R = 0.019$) for the transverse (longitudinal) resonance with a readout at the resonance maximum at 13.9 μm (15.9 μm), as indicated in Figure 7. A stronger signal ΔR can be obtained when the readout is done at the wavelength of the intersection of the two resonances, for the exemplary structure at 14.6 μm. Upon an increase in the refractive index, the transverse resonance will shift toward the readout point whereas the longitudinal resonance will shift away from it. Evaluating the variation in signal intensity, $\Delta R = 0.074$ is obtained. Hence, the measured signal ΔR is more than three times stronger for an evaluation at the wavelength of the intersection point than for an evaluation at the longitudinal resonance's wavelength. For an evaluation at the spectral position of the transverse resonance, the improvement is even higher.

6 Conclusions

We studied the polarization selective resonances of rectangular-shaped plasmonic nanoantennas made of highly doped InAsSb on GaSb substrates. The nanoantenna shape and material allow us to excite distinct longitudinal and transverse modes in the mid-IR. Switching between the spectral bands or excitation of all modes simultaneously is easily realized by the change of the polarization with respect to the resonator's axes. For the investigated array periodicities in the micrometer range, the nanoantennas behave as isolated objects. Yet, for large periodicities, it is possible to tune diffractive grating resonances to the spectral position of the LSPR. Strongest reflectance intensity is achieved for small array periodicities, thus densifying the nanoantennas on the substrate. We demonstrated the detection of vanillin molecules by characteristic IR absorption lines using the transverse and longitudinal LSPR to cover different spectral bands. Furthermore, we proposed an improved readout method for SPR sensing exploiting the overlap of the transverse and longitudinal LSPR. Ultimately, the plasmonic nanoantennas can be designed to cover precisely the spectral bands needed for the enhancement of the absorption features of interest for SEIRA spectroscopy for a targeted analyte, or for maximum readout for SPR sensing, using the appropriate nanoantenna dimensions.

Acknowledgments: This work was partially funded by the French Investment for the Future program (EquipEx EXTRA, ANR 11-EQPX-0016), by the French ANR (SUPREME-B, ANR-14-CE26-0015), by European Union's Horizon 2020 research and innovation programme (Marie Sklodowska-Curie grant agreement No. 641899) and by the Occitanie region. A. Mezy and M. Granier are acknowledged for helpful discussions about infrared spectroscopy. The authors thank Dr F. Neubrech for sharing his Eiler's smoothing program for the evaluation of SEIRA signals.

References

[1] Adato R, Yanik AA, Amsden JJ, et al. Ultra-sensitive vibrational spectroscopy of protein monolayers with plasmonic nanoantenna arrays. Proc Natl Acad Sci USA 2009;106:19227–32.
[2] Wu C, Khanikaev AB, Adato R, et al. Fano-resonant asymmetric metamaterials for ultrasensitive spectroscopy and identification of molecular monolayers. Nat Mater 2011;11:69–75.
[3] Li Y, Su L, Shou C, Yu C, Deng J, Fang Y. Surface-enhanced molecular spectroscopy (SEMS) based on perfect-absorber metamaterials in the mid-infrared. Sci Rep 2013;3:2865.
[4] Chen K, Dao TD, Ishii S, Aono M, Nagao T. Infrared aluminum metamaterial perfect absorbers for plasmon-enhanced infrared spectroscopy. Adv Funct Mater 2015;25:6637–43.
[5] Ogawa S, Fujisawa D, Hata H, Uetsuki M, Misaki K, Kimata M. Mushroom plasmonic metamaterial infrared absorbers. Appl Phys Lett 2015;106:41105.
[6] Tan SJ, Zhang L, Zhu D, et al. Plasmonic color palettes for photorealistic printing with aluminum nanostructures. Nano Lett 2014;14:4023–9.
[7] James TD, Mulvaney P, Roberts A. The plasmonic pixel: large area, wide gamut color reproduction using aluminum nanostructures. Nano Lett 2016;16:3817–23.
[8] Miyata M, Hatada H, Takahara J. Full-color subwavelength printing with gap-plasmonic optical antennas. Nano Lett 2016;16:3166–72.
[9] Muehlschlegel P, Eisler H-J, Martin OJF, Hecht B, Pohl DW. Resonant optical antennas. Science 2005;308:1607–9.
[10] Weber D, Albella P, Alonso-González P, et al. Longitudinal and transverse coupling in infrared gold nanoantenna arrays: long range versus short range interaction regimes. Opt Express 2011;19:15047–61.
[11] Novotny L. Optical antennas. Front Eng 2009;39:14–20.
[12] Aizpurua J, Bryant GW, Richter LJ, García De Abajo FJ, Kelley BK, Mallouk T. Optical properties of coupled metallic nanorods for field-enhanced spectroscopy. Phys Rev B Condens Matter Mater Phys 2005;71:1–13.
[13] Neubrech F, Kolb T, Lovrincic R, et al. Resonances of individual metal nanowires in the infrared. Appl Phys Lett 2006;89:253104.
[14] Muskens OL, Giannini V, Sánchez-Gil JA, Gómez Rivas J. Optical scattering resonances of single and coupled dimer plasmonic nanoantennas. Opt Express 2007;15:17736–46.
[15] Neubrech F, Pucci A, Cornelius TW, Karim S, García-Etxarri A, Aizpurua J. Resonant plasmonic and vibrational coupling in a tailored nanoantenna for infrared detection. Phys Rev Lett 2008;101:157403.
[16] Neubrech F, Weber D, Katzmann J, et al. Infrared optical properties of nanoantenna dimers with photochemically narrowed gaps in the 5 nm regime. ACS Nano 2012;6:7326–32.

[17] Viarbitskaya S, Demichel O, Cluzel B, Colas Des Francs G, Bouhelier A. Delocalization of nonlinear optical responses in plasmonic nanoantennas. Phys Rev Lett 2015;115:1–6.
[18] Nie ZH, Fava D, Kumacheva E, Ruda HE, Shik A. Plasmon spectra in two-dimensional nanorod arrays. Nanotechnology 2009;20:295203.
[19] Aksu S, Yanik AA, Adato R, Artar A, Huang M, Altug H. High-throughput nanofabrication of infrared plasmonic nanoantenna arrays for vibrational nanospectroscopy. Nano Lett 2010;10:2511–8.
[20] Bagheri S, Giessen H, Neubrech F. Large-area antenna-assisted SEIRA substrates by laser interference lithography. Adv Opt Mater 2014;2:1050–6.
[21] Mesch M, Metzger B, Hentschel M, Giessen H. Nonlinear plasmonic sensing. Nano Lett 2016;16:3155–9.
[22] Law S, Yu L, Rosenberg A, Wasserman D. All-semiconductor plasmonic nanoantennas for infrared sensing. Nano Lett 2013;13:4569–74.
[23] Law S, Adams DC, Taylor AM, Wasserman D. Mid-infrared designer metals. Opt Express 2012;20:12155–65.
[24] Baldassarre L, Sakat E, Frigerio J, et al. Midinfrared plasmon-enhanced spectroscopy with germanium antennas on silicon substrates. Nano Lett 2015;15:7225–31.
[25] Liu Z, Aydin K. Localized surface plasmons in nanostructured monolayer black phosphorus. Nano Lett 2016;16:3457–62.
[26] Tokumitsu E. Correlation between Fermi level stabilization positions and maximum free carrier concentrations in III-V compound semiconductors. Jpn J Appl Phys 1990;29(Part 2):L698–701.
[27] N'Tsame Guilengui V, Cerutti L, Rodriguez J-B, Tournié E, Taliercio T. Localized surface plasmon resonances in highly doped semiconductors nanostructures. Appl Phys Lett 2012;101:161113.
[28] Lee K, El-sayed MA. Gold and silver nanoparticles in sensing and imaging: sensitivity of plasmon response to size, shape, and metal composition. J Phys Chem B 2006;110:19220–5.
[29] Bharadwaj P, Deutsch B, Novotny L. Optical antennas. Adv Opt Photonics 2009;1:438.
[30] Zayats AV, Smolyaninov II, Maradudin AA. Nano-optics of surface plasmon polaritons. Phys Rep 2005;408:131–314.
[31] Liu Z, Boltasseva A, Pedersen RH, et al. Plasmonic nanoantenna arrays for the visible. Metamaterials 2008;2:45–51.
[32] Huck C, Neubrech F, Vogt J, et al. Surface-enhanced infrared spectroscopy using nanometer-sized gaps. ACS Nano 2014;8:4908–14.
[33] Barho FB, Gonzalez-Posada F, Milla-Rodrigo M-J, Bomers M, Cerutti L, Taliercio T. All-semiconductor plasmonic gratings for biosensing applications in the mid-infrared spectral range. Opt Express 2016;24:16175–90.
[34] Taliercio T, Guilengui VN, Cerutti L, Tournié E, Greffet J-J. Brewster "mode" in highly doped semiconductor layers: an all-optical technique to monitor doping concentration. Opt Express 2014;22:24294–303.
[35] Milla MJ, Barho F, González-Posada F, et al. Localized surface plasmon resonance frequency tuning in highly doped InAsSb/GaSb one-dimensional nanostructures. Nanotechnology 2016;27:425201.
[36] Degiron A, Lezec HJ, Yamamoto N, Ebbesen TW. Optical transmission properties of a single subwavelength aperture in a real metal. Opt Commun 2004;239:61–6.
[37] Garcia-Vidal FJ, Martin-Moreno L, Ebbesen TW, Kuipers L. Light passing through subwavelength apertures. Rev Mod Phys 2010;82:729–87.
[38] D'Andrea C, Bochterle J, Toma A, et al. Optical nanoantennas for multiband spectroscopy. ACS Nano 2013;7:3522–31.
[39] Ming T, Zhao L, Yang Z, et al. Strong polarization dependence of plasmon-enhanced fluorescence on single gold nanorods. Nano Lett 2009;9:3896–903.
[40] Calculations were performed with the commercial software Lumerical FDTD Solutions version 8.12, Lumerical Solutions Inc.
[41] Meier M, Wokaun A. Enhanced fields on rough surfaces: dipolar interactions among particles of sizes exceeding the Rayleigh limit. J Opt Soc Am B 1985;2:931–49.
[42] Lamprecht B, Schider G, Lechner RT, et al. Metal nanoparticle gratings: influence of dipolar particle interaction on the plasmon resonance. Phys Rev Lett 2000;84:4721–4.
[43] Haynes CL, Mcfarland AD, Zhao L, et al. Nanoparticle optics: the importance of radiative dipole coupling in two-dimensional nanoparticle arrays. J Phys Chem B 2003;107:7337–42.
[44] Nordlander P, Oubre C, Prodan E, Li K, Stockman MI. Plasmon hybridization in nanoparticle dimers plasmon hybridization in nanoparticle. Nano Lett 2004;4:899–903.
[45] Bouhelier A, Bachelot R, Im JS, et al. Electromagnetic interactions in plasmonic nanoparticle arrays. J Phys Chem B 2005;109:3195–8.
[46] Chae J, Lahiri B, Centrone A. Engineering near-field SEIRA enhancements in plasmonic resonators. ACS Photonics 2016;3:87–95.
[47] Abb M, Wang Y, Papasimakis N, de Groot CH, Muskens OL. Surface-enhanced infrared spectroscopy using metal oxide plasmonic antenna arrays. Nano Lett 2013;14:346–52.
[48] Neubrech F, Huck C, Weber K, Pucci A, Giessen H. Surface-enhanced infrared spectroscopy using resonant nanoantennas. Chem Rev 2017;117:5110–45.
[49] Hartstein A, Kirtley JR, Tsang JC. Enhancement of the infrared absorption from molecular monolayers with thin metal overlayers. Phys Rev Lett 1980;45:201–4.
[50] Vogt J, Huck C, Neubrech F, Toma A, Gerbert D, Pucci A. Impact of the plasmonic near- and far-field resonance-energy shift on the enhancement of infrared vibrational signals. Phys Chem Chem Phys 2015;17:21169–75.
[51] Valdez-Flores C, Can MP. Food chemistry on-line dilution and detection of vainillin in vanilla extracts obtained by ultrasound. Food Chem 2007;105:1201–8.
[52] Farthing D, Sica D, Abernathy C, et al. High-performance liquid chromatographic method for determination of vanillin and vanillic acid in human plasma, red blood cells and urine. J Chromatogr B 1999;726:303–7.
[53] Chalmers JM, Griffiths PR. Handbook of vibrational spectroscopy. Chichester, Wiley, 2002.
[54] Giannini V, Francescato Y, Amrania H, Phillips CC, Maier SA. Fano resonances in nanoscale plasmonic systems: a parameter-free modeling approach. Nano Lett 2011;11:2835–40.
[55] Eilers PHC. A perfect smoother. Anal Chem 2003;75:3631–6.
[56] Guyot L, Patskovsky S, Meunier M. Integrated silicon-based nanoplasmonic sensor. Opt Express 2011;19:9962–7.
[57] Piliarik M, Homola J. SPR sensor instrumentation. In: Homola J, ed. Surface plasmon resonance based sensors. Berlin and Heidelberg, Springer, 2006, 45–67.

Supplemental Material: The online version of this article offers supplementary material (https://doi.org/10.1515/nanoph-2017-0052).